Plume detection and estimate emissions for biomass burning plumes from TROPOMI Carbon monoxide observations using APE v1.0

Manu Goudar[1], Juliëtte Anema[2], Rajesh Kumar[3], Tobias Borsdorff[1], and Jochen Landgraf[1]

[1]SRON Netherlands Institute for Space Research, Leiden, The Netherlands
[2]Royal Netherlands Meteorological Institute (KNMI)
[3]National Center for Atmospheric Research (NCAR)

Correspondence: Manu Goudar (manugv@sron.nl)

Abstract. The TROPOspheric Monitoring Instrument (TROPOMI) onboard the Sentinel-5 Precursor (S-5P) satellite, launched in 2017, measures the total column concentration of the trace gas Carbon Monoxide (CO) daily on a global scale and at a high spatial resolution of 7×7 km^2, improved to 5.5×7 km^2 in August 2019. The TROPOMI observations show plumes of CO due to localized CO emissions from industrial sources and biomass burning. In this paper, we quantify these CO emissions for

5 biomass burning by an automated algorithm, APE, to detect plumes and quantify the CO emission rate using cross-sectional flux method. Furthermore, the influence of a constant and a varying plume height in downwind direction on emissions is investigated and algorithm uncertainties are quantified. The VIIRS active fire data in conjunction with the TROPOMI CO datasets is used to identify fires and the fire locations. Then, an automated plume detection algorithm using traditional image processing algorithms is developed and utilized to identify plumes. For these plumes, the emission rate is estimated by the cross-

10 section flux method at three different plume heights. The first two are constant plume heights at a 100 m and an IS4FIRES injection height from Global Fire Assimilation System. And the last one is a varying plume height in downwind direction. A 3D Lagrangian model is used to simulate tracer particles where the source locations for the simulation are based on the VIIRS fire counts and IS4FIRES injection height. 3D velocities at 137 model levels (ERA5) are utilized to simulate tracer particles. We demonstrate the quality and validity of our automated approach by investigating biomass burning events and their

15 emissions for Australia on Oct 2019 and the US on Sept 2020. A total of 110 and 31 individual fire plumes in Australia and the US, respectively were detected and their emissions estimated. The emissions were severely under-predicted and negative for 11 cases when based on constant plume height of 100 m compared to emissions based on varying plume height. Furthermore, the effect of the changing plume height in downwind direction on the emission estimate compared to emissions from constant IS4FIRES plume height was minor as 124 cases are found to have emission variation less than 10%. However, we were able to

20 identify several cases where the flux estimates become more reliable with varying plume height. Thus, the varying plume height in downwind direction is considered for the automated algorithm. The cross-section flux method is found to have an uncertainty of 38% in one of the idealized cases. However, overall uncertainty of the algorithm is difficult to quantify as conditions for each fire are unique.

1 Introduction

25 Carbon monoxide (CO) is an air pollutant and in high concentrations, it causes harmful health effects. Moreover, it is a weak greenhouse gas and an indirect contributor to increase in several greenhouse gases in the atmosphere (Spivakovsky et al., 2000). CO is produced mainly due to incomplete combustion. For example, biomass burning (Andreae et al., 1988; Watson et al., 1990) increases CO in atmosphere and Shi et al. (2015) quantified the total CO emissions from vegetation burning, fuel-wood combustion, and human waste for three tropical regions. Also, Granier et al. (2011); Crippa et al. (2018); Hoesly 30 et al. (2018) show that the CO emissions due fossil fuel burning has been on increase since 2000. Additionally, CO emitted by localized sources at the ground leads to a prominent footprint in the atmosphere, namely plumes, due to its lifetime from days to several months (Holloway et al., 2000). Thus, it becomes essential to understand the effect of CO on air-quality and climate by measuring it accurately on a global and local scales which helps to quantify CO emissions.

The TROPOspheric Monitoring Instrument (TROPOMI) aboard the Sentinel-5 Precursor (S5P) satellite launched in 2017, 35 monitors CO daily on global scale (Borsdorff et al., 2018) and at a high spatial resolution of $7 \times 7 \ \mathrm{km}^2$, improved to $5.5 \times 7 \ \mathrm{km}^2$ in August 2019. Rowe et al. (2022) compared the TROPOMI CO measurements to aircraft measurements for biomass burning plumes in 2018 and found that the difference between two measurements is about 7.2%. Furthermore due to TROPOMI's high spatial resolution and the daily coverage of the TROPOMI CO Level-2 dataset, the CO emissions by cities (Borsdorff et al., 2019a, 2020; Lama et al., 2020), wildfires (Schneising et al., 2020; Li et al., 2020; Magro et al., 2021; van der Velde et al., 40 2021) and industrial sources (Tian et al., 2021) have been quantified and studied. Most of these studies estimate CO flux on large-scale regions (Schneising et al., 2020; Magro et al., 2021; van der Velde et al., 2021) and mega-city scales (Borsdorff et al., 2019a, 2020; Lama et al., 2020). However, not many single point emissions are quantified from the TROPOMI CO dataset. Tian et al. (2021) showed CO emissions based on TROPOMI for single point industrial sources from India and China. A similar approach has not been shown for biomass burning (fires) single point sources in the literature. The geo-locations of 45 the industrial sources in Tian et al. (2021) are known a priori, whereas the locations for fire events are not known in advance and are not fixed in time. The Visible Infrared Imaging Radiometer Suite (VIIRS) 375m thermal anomalies/active fire product (Schroeder et al., 2014) can be used to detect single point sources. The VIIRS instrument is aboard the joint NASA/NOAA Suomi National Polar-orbiting Partnership (Suomi NPP) satellites, which flies in the same orbit as S5P in loose formation with a temporal separation of 3.5 minutes between them. The collocated observations of TROPOMI and VIIRS are presently used 50 for cloud clearing of the S5P methane data product (Lorente et al., 2021) and in a similar manner, the VIIRS active fire data product will be used in this study to identify the locations of fires.

The CO plumes in the TROPOMI data can be used to estimate CO emission by wild fires and different methods are discussed in the literature, namely, the inversion methods coupled with Gaussian dispersion models (Krings et al., 2011; Nassar et al., 2017; Lee et al., 2019) or different Chemical Transport Models (CTM) (Brasseur and Jacob, 2017), Cross-sectional Flux 55 Methods (CFM) (White et al., 1976; Beirle et al., 2011; Cambaliza et al., 2014, 2015; Kuhlmann et al., 2020) and integrated mass enhancement (IME) method (Frankenberg et al., 2016). The inversion coupled with a Gaussian plume model is simple where an analytically computed Gaussian plume is fitted to TROPOMI CO column observations. Here, wind conditions are

assumed to be steady and uniform which might not be true for the fires. This can cause large deviations between the instantaneous plumes and the computed steady-state Gaussian plume (Varon et al., 2018). The inversion methods using CTMs, such

60 as Weather Research and Forecasting model coupled to Chemistry (WRF-Chem) (Grell et al., 2005), GEOS-Chem (Bey et al., 2001), and others can reduce uncertainties thereby predicting emissions more accurately. However, the corresponding simulations are complex, computationally expensive and difficult to automate, in particular for a large number of fires with different geolocations which is the objective of this study. The CFM needs comparatively less computational power and is easier to automate. It is based on the mass conservation of the pollutant transport in downwind direction of the plume. The CO emission is

65 estimated from corresponding fluxes across different planes perpendicular to the direction of plume using the the wind velocity at the plume height. The plume height depends upon different aspects, namely, meteorology, emission height, etc (Brunner et al., 2019) and may not be explicitly available. Moreover, the CFM breaks down when diffusion is dominant, i.e, when the velocity is $< 2 \, \mathrm{ms}^{-1}$ (Varon et al., 2018).

The present work aims at developing an automated plume detection and emission estimation scheme for CO flux inversion

70 for fires. For this purpose, we employ and improve the CFM as it has the potential to be applied in an operational data processing. First, VIIRS fire data and satellite data are prepared for automated plume detection which is discussed in section 2.1. Plume detection algorithm from a single point source using VIIRS fire counts is the subject of section 2.2. Section 2.3 describes emission estimation using cross-sectional flux method where an appropriate choice of the plume height and the wind fields are discussed. The study results will be deliberated in Section 3 and finally Section 4 concludes our study and sets

75 recommendations for the future work.

2 Methodology

Figure 1 illustrates a high-level flowchart of our Automated Plume detection and Emission estimation algorithm (APE). It is divided into three parts, namely data preparation, automatic plume detection, and emission estimation. During data preparation, the algorithm identifies single point fire sources from VIIRS 375 m active fire data product (Schroeder et al., 2014) and

80 subsequently selects and extracts a TROPOMI CO data around the located fire sources. The plume detection algorithm searches for a plume in the extracted CO data which is required as an input for emission estimation. The emission estimation algorithm initially computes the background CO which is the usual observed CO concentration at that location without any CO emissions due to the fire. Subtracting the background allows us to obtain the enhanced CO which further is used to estimate the emissions by cross-sectional flux method. These three parts of the algorithm are discussed in the following sections.

2.1 Data preparation

2.1.1 Selection of fire events

Fire events can be inferred from the VIIRS 375m active fire data product (Schroeder et al., 2014) provided by LANCE FIRMS which is operated by NASA ESDIS (https://earthdata.nasa.gov/active-fire-data). The data contains different parameters such
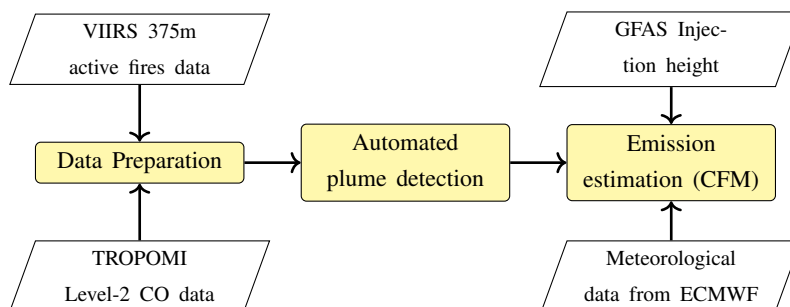
Figure 1. High-level flow chart of the APE algorithm.

as fire radiative power (FRP), temperature and the time of measurement defined at latitude-longitude coordinates which corre-
90 spond to the center of a $375 \times 375 \text{ m}^2$ ground pixel. Furthermore, each of these latitude-longitude coordinates will be referred
to as a fire count in this paper. Mostly, an emission plume created by a burning in a single VIIRS pixel cannot be detected by
Tropomi with a pixel size of $7 \times 7 \text{ km}^2$. And only a cluster of VIIRS fire counts can lead to a detectable CO plume in the ob-
servations. To identify such clusters, we employ the Density-Based Spatial Clustering of Applications with Noise (DBSCAN)
(Ester et al., 1996; Schubert et al., 2017) algorithm from the scikit-learn library (Pedregosa et al., 2011). It separates the areas
95 densely packed with fire counts from the low dense areas and has an ability to detect arbitrarily-shaped clusters. DBSCAN
requires two inputs, first the maximum search radius, r_{max}, around a fire count and second the minimum number of fire counts
within the area, $n_{\min}$. r_{max} is set to 4 km which is approximately half of the TROPOMI pixel size. The minimum number of
fire counts have been set to $n_{\min} = 10$. Figure 2 illustrates the data selection of 63 clusters based on VIIRS fire counts on 6
October, 2019. For further analyses, we convert each cluster to a single point source using fire radiative power (FRP) as weights
100 of the individual fire counts. This single point source will be referred to as fire source from now on and serves as an input to
TROPOMI CO data preparation.

2.1.2 TROPOMI CO data preparation

For the identified fire sources from VIIRS data, the corresponding TROPOMI orbit (L2 product version 1.03.02) is selected.
Figure 3 illustrates the collocated information for a data granule over Australia. The orbit is corrected for stripes (see Fast
105 Fourier Transformation algorithm of Borsdorff et al. (2019b)). For each fire source, we extract a 41×41 pixel granule of
TROPOMI CO data centered around the source by applying two data quality filters. First, the maximum pixel size due to
distortion in swath direction is constrained to < 12 km to avoid large pixel size and its variation within the granule. The second
data filter is based on number of pixels that satisfy the data quality value, (1) in the extracted 41×41 pixels granule and (2) in
7×7 pixels granule centered around the fire source. The data quality value (q_a) is given in the TROPOMI L2 product (Apituley
110 et al., 2018) per ground pixel. If 80% and 85% ground pixels have $q_a > 0.5$ in the extracted 41×41 and 7×7 pixels granules,
respectively, then the extracted CO granule is considered good. The selected CO scene is forwarded as an input to the plume
detection algorithm.
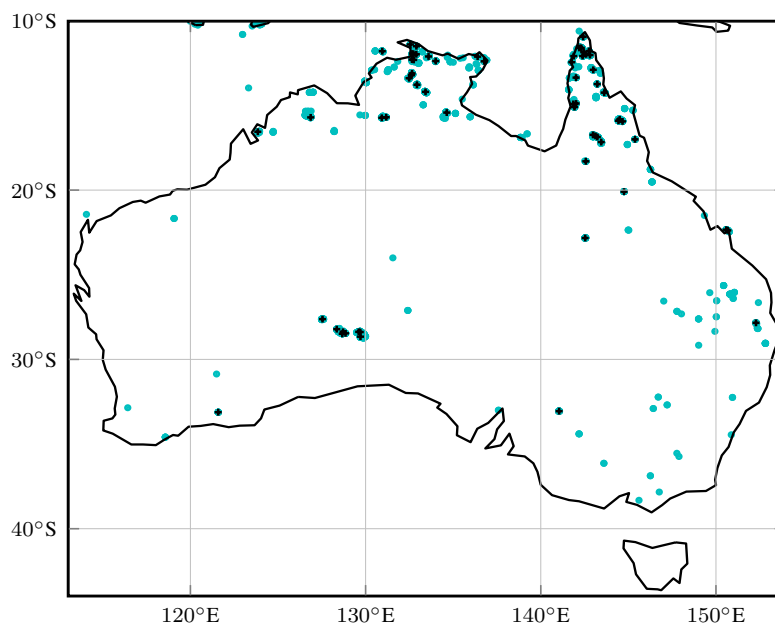
Figure 2. Fire counts on 2019-10-06. Cyan color depicts fire-counts that were not clustered and black '+' markers represent a total of 63 clusters determined by DBSCAN algorithm.

2.2 Plume detection algorithm

Within each selected CO data granule, we try to identify a plume. Kuhlmann et al. (2019) developed a plume detection al-

115 gorithm based on statistical methods and Finch et al. (2021) used machine learning to detect plumes. A machine learning approach is not considered in the present study mainly due to non-availability of gold standard data. Instead, our plume detection approach is based on traditional image processing algorithms (van der Walt et al., 2014).

Using the extracted CO TROPOMI data, a plume is detected by a region-based segmentation algorithm where pixels with similar properties are clustered together to form a homogeneous region. One of the most commonly used and classic region-

120 based segmentation algorithm is the 'marker based watershed transform method' (Beare, 2006; Gao et al., 2004). The CO column concentration represents metaphorically the altitude of a topographic map. Thus, the watershed algorithm segments the regions into valleys and mountains (CO enhancements) based on a given marker. In the following we describe the plume detection in more detail using an example.

The marker-based watershed algorithm in the scikit-image package (van der Walt et al., 2014) takes two inputs to segment an

125 image, one is the 'elevation map' $\mathbf{I}_{\mathrm{elev}}$ where the changes in altitude are emphasized and homogeneous regions are dampened. The second input is a marker image $\mathbf{I}_{\mathrm{mark}}$ which provides the seed points referred by an integer label for the algorithm. The definition of both inputs is discussed in the following paragraphs.
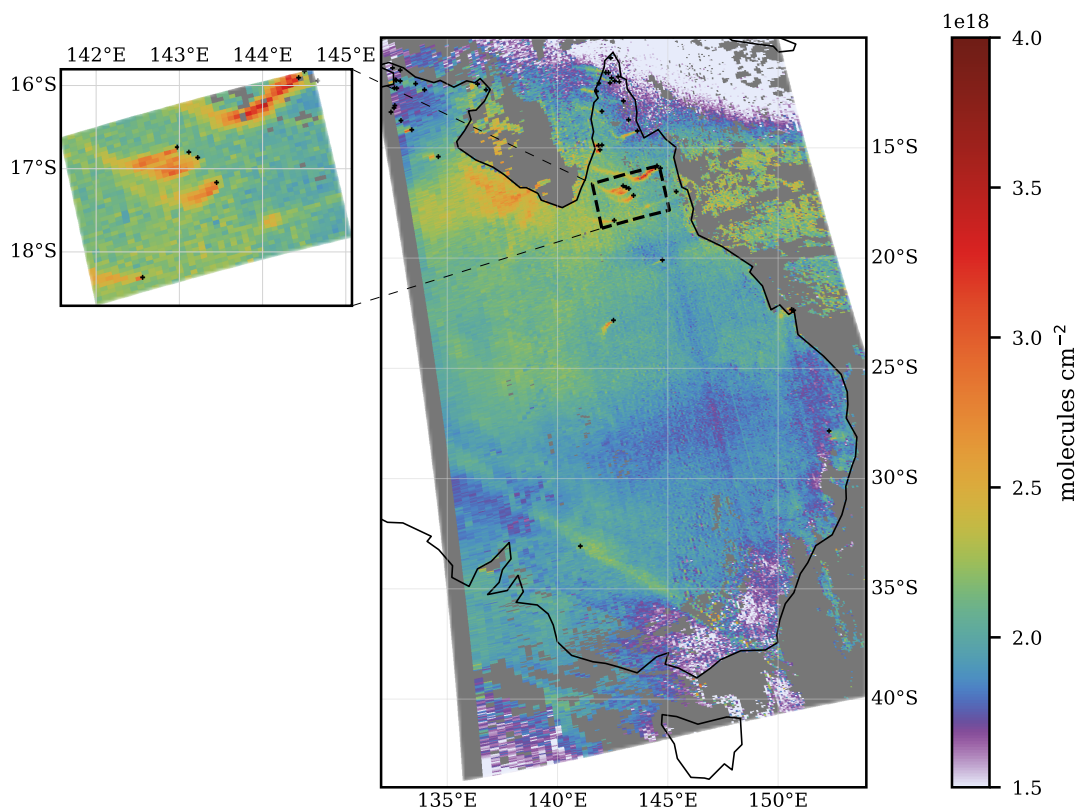
Figure 3. 49 detected fire sources represented by black '+' on 2019-10-06 overlapped with the TROPOMI level 2 CO data for orbit 10254. The dashed region represents a 41×41 pixel granule.

We start with the extracted CO TROPOMI granule of a 41×41 pixel size $\mathbf{I}(i,j)$ with $i,j = 1, \cdots, 41$. An example is shown in Figure 4(a). First, high frequency components of the CO-image are reduced by a Gaussian filter. The smoothened image is referred to as $\mathbf{I}_s$. From this image, the elevation map $\mathbf{I}_{\mathrm{elev}}$ is computed using a Sobel operator (Sobel and Feldman, 1990; van der Walt et al., 2014) which is a discrete differentiation operator, computing an approximation of the gradient of the image to emphasizes edges as shown in Figure 4b.

By default the marker image ($\mathbf{I}_{\mathrm{mark}}$) is initiated by

$$\mathbf{I}_{\mathrm{mark}}(i,j) = 0 \quad \forall \quad i,j = 1, \cdots, 41 \tag{1}$$

Next, we define two different seeds. $\mathbf{I}_{\mathrm{mark}}(i,j) = 1$ indicates regions which do not have a CO enhancements and $\mathbf{I}_{\mathrm{mark}}(i,j) = 2$ refers to regions of clear CO enhancements. Regions of no CO enhancements are identified by the median M, of $\mathbf{I}_S$ and a
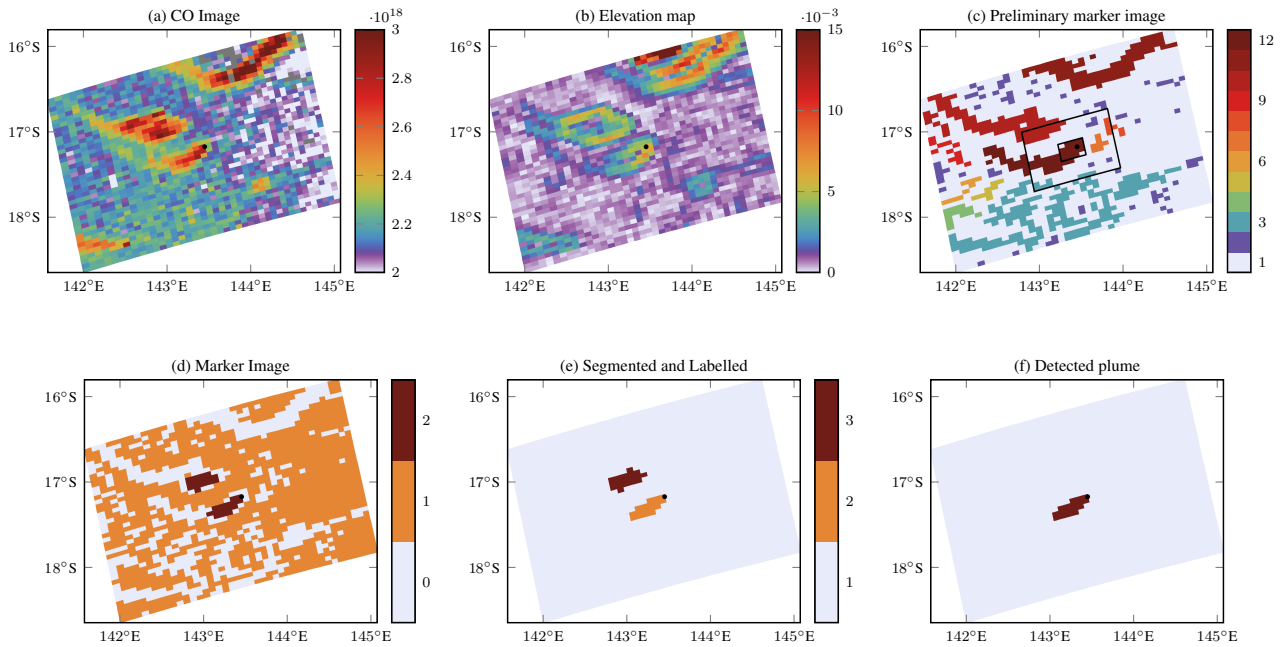
Figure 4. Plume detection algorithm. Figure shows different steps of the algorithm for an example plume for a fire on 6th October 2019 in Australia.

dynamically computed threshold $\mathbf{I}_{\mathrm{DT}}$, namely

$$\mathbf{I}_{\mathrm{mark}}(i,j) = 1 \quad \text{when} \quad \mathbf{I}_{\mathrm{S}}(i,j) \leq M(\mathbf{I}_{\mathrm{S}}) \quad \text{or} \quad \mathbf{I}_{\mathrm{S}}(i,j) \leq \mathbf{I}_{\mathrm{DT}}(i,j)$$

$$\text{where} \quad \mathbf{I}_{\mathrm{DT}}(i,j) = \frac{1}{(2N+1)^2} \sum_{i'=i-N}^{i+N} \sum_{j'=j-N}^{j+N} \mathbf{I}_{\mathrm{S}}(i',j') \tag{2}$$

140 with $N = 7$. Thus each pixel in $\mathbf{I}_{\mathrm{DT}}$ represents a localized mean of 15×15 pixels. For our example in Figure 4, the corresponding region is shown by the color represented by label '1' in Figure 4c.

Using this preliminary marker image, we identify all the connected regions using the 'label' algorithm (Fiorio and Gustedt, 1996) in the scikit-image (van der Walt et al., 2014) and assign an unique label to each region shown in different colors in Fig 4c. Further, in a 5×5 pixel area around the fire source, we extract the labels of all connected regions as the potential plume

145 areas. In Fig. 4c, there is only one connected region which corresponds to label '12' (dark red color). Next, all the pixels (dark red pixels) corresponding to the extracted label '12' within a 15×15 pixel area around the fire source are extracted. Finally, we calculate the upper threshold as the mean of these extracted pixels. This yields the remaining seed points which are defined only in a 15×15 pixel area around the fire source as shown below

$$\mathbf{I}_{\mathrm{mark}}(i,j) = 2 \quad \text{when } \mathbf{I}_{\mathrm{S}}(i,j) \geq \text{upper threshold} \quad \text{for} \quad i,j = 14,\ldots,28. \tag{3}$$

150 The final marker image is shown in Figure 4d.

Finally, the watershed algorithm calculates a segmented image using the elevation map image $\mathbf{I}_{\text{elev}}$ and the marker image $\mathbf{I}_{\text{mark}}$. Each region in segmented image is uniquely labeled as shown in Figure 4e. Further, the segmented image is checked for the existence of a plume. At first, the regions present in the center 7×7 pixels are extracted and for all these regions, the total number of pixels and the maximum length of each region with respect to the source location are computed. The region, R, with maximum length is selected and is identified as plume if it satisfies the following four constrains

- The number of pixels in R should be > 5

- The maximum length should be > 40 km

- There should be no other identified fire clusters within $0.1°$ distance from the plume

- There should be no 10 non-clustered or 20 both clustered or non-clustered fire counts within $0.05°$ distance from or in the plume

With the first and second constrain, small plumes are filtered and the third and fourth constrains alleviate the overlapping of fires from different fire sources. A detected plume of our example is illustrated in Figure 4f.

2.3 Emission estimation

For the detected plumes, the emissions were estimated using the cross-sectional flux method (CFM). The CO emission E is defined as the mean flux through n cross sections perpendicular to the downwind direction of the plume, namely

$$E = \frac{1}{n} \sum_{i=1}^{n} Q_i$$
$$Q_i = \int \delta C_{\text{co}}^i(s, t_0) \cdot u^i(z_i, s, t_0) \cdot ds \qquad (4)$$

where Q_i (in kgs^{-1}) is the CO flux through cross section i, δC_{co}^i (in kgm^{-2}) is the background subtracted CO values along a cross-section i and u^i (in ms^{-1}) is the velocity perpendicular to the cross-section i. The wind velocity $u(z, s, t_0)$ at the plume height z, the cross-section position s and at the observation time t_0 is obtained from the European Center for Medium range Weather Forecasts (ECMWF) Reanalysis v5 (ERA5) data (Hersbach et al., 2018b). For error characterization, we define the standard error as

$$\sigma_{\text{E}} = \frac{1}{n} \sqrt{\sum_{i=1}^{n} (E - Q_i)^2} \qquad (5)$$

To determine the cross-sections, hereafter referred to as transects, we first calculate the direction of the plume in downwind direction. The plume line results from a second order curve fit through the pixel centers of the identified pixels (see e.g. the black solid line in Fig. 5a). Next, we calculate the transects at every 2.5 km perpendicular to the plume line which is illustrated as dashed lines in Figure 5a. To calculate Q_i in Eq. 4, each transect is sampled at distances of 500 m.

(a)   (b)   (c)
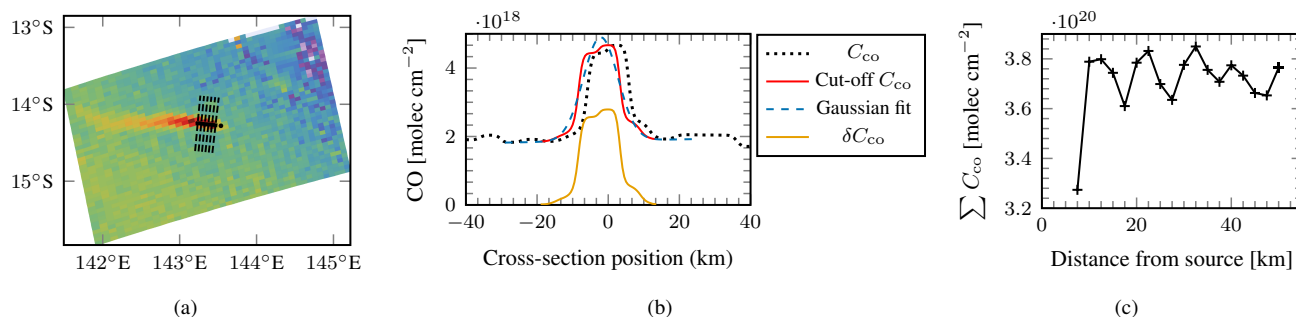
Figure 5. Plume on 2019-05-19 at 04:55 UTC. (a) Plume and every second transaction lines drawn based on the detected plume separated by 5 km in downwind direction. (b) The black dotted line corresponds to CO column along a transect in (a) and the red line shows recentered and cut-off CO used for Gaussian fitting. Blue-dash dotted line corresponds to the Gaussian fit and orange line represents the enhanced CO along the transect. (c) $\sum C_{\mathrm{co}}$ along a transect against the distance from source. (d) Background subtraction algorithm fails due to two plumes merging.

Along each transect, the CO column (C_{co}) is extracted by linear interpolation of the original CO data and is illustrated by dotted black line in Figure 5b. This CO column is further used to compute δC_{co} in Eq. 4. During the diagnostics tests

180   of our interpolation algorithm, an oscillation was observed in the CO columns integrated along the transects as a function of the downwind distance from the fire source (see Figure 5c). The oscillation is due to interpolation errors from the large sized pixels. The distance between two minima is approximately equal to the TROPOMI pixel size. This error is found to propagate further into the CO enhancement δC_{co} which is computed from background subtraction algorithm.

2.3.1 Background Subtraction

185   To determine the atmospheric background of CO per transect, first we re-center the C_{co} such that the maximum is at the origin. Then the transect line is truncated at the first minima of CO on either side of the origin as illustrated by red line in the Fig. 5b. To determine the background for each transect (red line), we assume that the column CO along the transect can be expressed as

$$C_{\mathrm{co}} = H_0 + H_1 \cdot s + A_0 G(s) \tag{6}$$

190   where $C_{\mathrm{co}}^b = H_0 + H_1 \cdot s$ describes a linear CO background per transect and the Gaussian G accounts for the CO enhancement. We determine the background by fitting Eq. 6 through the CO data, which we subsequently subtract from the C_{co} data to calculate the CO enhancement

$$\delta C_{\mathrm{co}} = \max\{0,\ C_{\mathrm{co}} - H_0 + H_1 \cdot s\}. \tag{7}$$

Here, the negative CO column enhancements are ignored. The blue dashed line and the orange line in Fig. 5b represent Gaussian
195   fit and δC_{co}, respectively.

2.3.2 Filtering during background subtraction
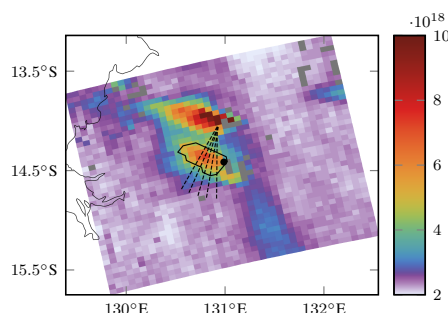
Figure 6. Background subtraction algorithm fails due to two plumes merging.

The background subtraction includes an important filtering mechanism to remove overlapping fires. Figure 6 shows a plume highlighted by the black polygon and two overlapping fires from different fire sources. It is difficult to separate these two plumes completely, thus, in present study these cases are filtered out. This is done during the background subtraction after the transect line is truncated. If the difference between two minima on either side of a truncated transect is higher than 10%, then the transect is flagged as bad. It should also be noted that the estimation of background CO might go wrong when the difference on two sides of transect is high. For the plume in Fig. 6, all the transects at least have a difference of 25%, thus the plume is rejected and filtered out.

2.3.3 Plume height

The plume height z_i at a transect/cross-section i is used to extract the appropriate wind velocity $u(z_i, s, t_0)$. For wildfires, Rémy et al. (2017) showed that the IS4FIRES injection height, z_{inj}, from the Global Fire Assimilation System (GFAS) database is in a good agreement with the observations. The uncertainty in injection height is about 500 m (Sofiev et al., 2012). First, we assume that the plume height is equal to z_{inj} and is constant throughout the plume, which may hold true for stable meteorological conditions. The constant plume height will be referred as z_{c} and uncertainty at this plume height is given as z_{c}^p and z_{c}^m which correspond of $z_{\mathrm{inj}} + 500$ m and $z_{\mathrm{inj}} - 500$ m, respectively.

It should be noted that the injection computed in GFAS is for 24 h and may not be appropriate for a satellite plume which is a snapshot at time t_0. Additionally, the plume height might vary due to meteorology in downwind direction. Therefore, we simulated alternatively particle trajectories starting at the fire location around the injection height with a three dimensional Lagrangian tracer dispersion model. This allows us to estimate the local plume height z_i by a vertical averaging of tracers along the downwind direction. The estimated plume height is referred as z_{lag} in the following, which captures the change in height in the downwind direction.

The Lagrangian simulations are performed using tracer particles. The motion of tracers is simulated according to

$$\frac{d\mathbf{x}_p(t)}{dt} = \mathbf{v}(\mathbf{x}_p(t)) \tag{8}$$
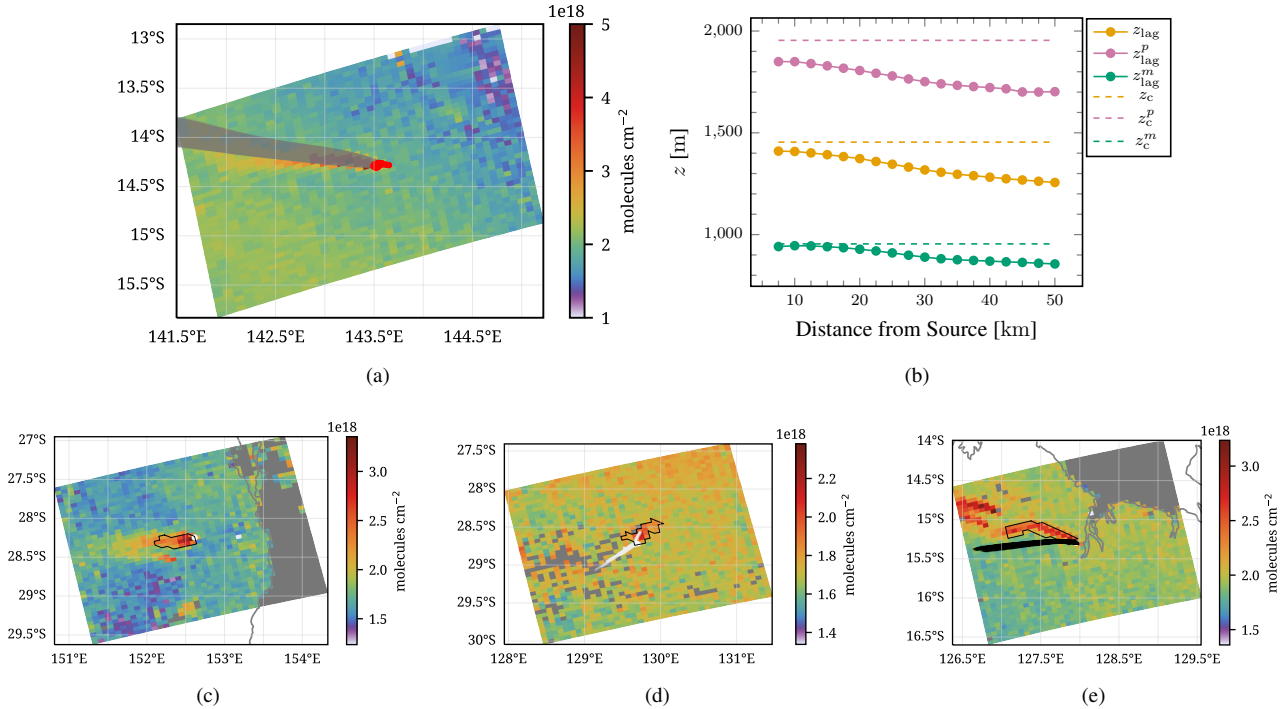
Figure 7. (a) The grayish band shows all tracer particles at the end of Lagrangian simulation and the red dots show the fire counts on the detected plume. (b) Shows the plume height computed for different transects from Lagrangian simulations. The constant plume height (z_c) represented by orange dashed line is 1454.3 m. (c) Detected plume is represented by the polygon in black line and the injection height was found to be zero for this case. (d) An example where the particles are not aligned with the plume. (e) Particle trajectories are slightly rotated compared to plume.

where $\mathbf{v}(\mathbf{x}_p)$ represents the fluid velocity at the instantaneous particle position $\mathbf{x}_p$. The explicit forward Euler scheme is
220 employed to integrate the equation in time. The velocity on the right-hand side is calculated by the tri-linear interpolation of the ERA5 velocity fields. The source locations for the Lagrangian simulations are based on the fire counts described in Section 2.1.1. At each source location, 3 tracer particles are released at z_{inj} and $z_{\mathrm{inj}} \pm 500$ m and the particle trajectories are simulated. Particles are released at $z_{\mathrm{inj}} \pm 500$ m for uncertainty analysis. The end time of the simulations is the TROPOMI measurement time t_0 and the simulation start is $t_0 - 6$ h. The particles are released from the source locations every 2 minutes. Figure 7(a)
225 shows the tracer particle simulation for a plume and the grayish band indicates them at TROPOMI measurement time.

At each intersect, the height of the tracer particles released at z_{inj} are extracted and the mean height, $z_{\mathrm{lag},i}$ is computed. The mean height or plume height is assumed to be constant along the transect. Figure 7(b) shows the plume height for different transects from the fire source which is used to compute velocity, u, in Equation 4. The uncertainty in plume height is defined as z_{lag}^p and z_{lag}^m and are computed from tracer particles that were released at height $z_{\mathrm{inj}} + 500$ m and $z_{\mathrm{inj}} - 500$ m, respectively
230 and can be observed in Figure 7(b). Finally, the velocity, u, is used to compute emissions.

2.3.4 Filtering during Lagrangian simulations

During the Lagrangian simulation, we apply three filters, two of them are before the start of the simulation and one is done after the simulation. These filters are described below.

The injection height in GFAS is not always available for all the detected plumes and these cases are ignored. This can
235 happen due to false detection of plume or false fire in VIIRS active fire database or just the data is missing in GFAS database. Figure 7(c) shows a case where there is a plume but no data for injection height was available. Additionally, the fire radiative power (FRP) for this case was found to be comparable to other detected plumes with the non-zero injection height. This can be attributed to either false detection of fire in VIIRS dataset or missing data in GFAS database.

The second filter is after the Lagrangian simulations where the particle-plume alignment is checked. If the particles are not
240 aligned in the direction of the plume then the plume is rejected (see Fig. 7(d)). Sometimes the particle trajectory was observed to have a slight rotation from the plume as illustrated in Fig. 7(e). This can be due to the rotation or the errors in the ERA5 velocities or due to the spatial and temporal resolution of velocity fields or inaccurate injection height. However, such cases were considered when the particle trajectories overlapped with the transaction lines.

The third filter is based on velocities. If the velocity at the TROPOMI measurement time which is used to compute emissions
245 is less than 2 ms^{-1} then the plume is rejected with the assumption that the diffusion dominates the pollutant transport.

3 Algorithm application

Table 1. Results for automated plume detection and emission estimation algorithm (APE v1.0) for two months in US and Australia

Location	Fire Clusters	CO data	Plume detection	Emission estimation	Visual Inspection
US	1081	228	64	33	31
Australia	2013	394	132	111	110
Total cases	3094	622	196	144	141

The quality and validity of the algorithm, APE v1.0, is illustrated for fire sources in Australia (AU) on October 2019 and the United States of America (US) on September 2020. These months were chosen as large number of fires were observed during this time. Table 1 shows the result of our automated plume detection and emission estimation. A total of 3094 fire clusters were
250 detected in the VIIRS active fire data product for both US and Australia based on the method discussed in 2.1.1. TROPOMI CO overpasses were then identified and the CO data was filtered for quality (see Sec. 2.1.2) which resulted in 622 cases with good TROPOMI CO data. Furthermore, the plume detection algorithm described in Sec. 2.2 identified 196 plumes among 622 cases. The emission estimation algorithm computed emissions using CFM for a total of 144 plumes. So about 52 cases were filtered by emission estimation algorithm. At first, the injection height filter described in Sec. 2.3.4 led to removal of 19 cases
255 (10 US and 9 AU). Then a total of 9 cases (7 US and 2 AU) were found to be overlapping with another plume from different fire source and were flagged as bad plumes during background subtraction (see Sec. 2.3.2). Furthermore particles-plume alignment
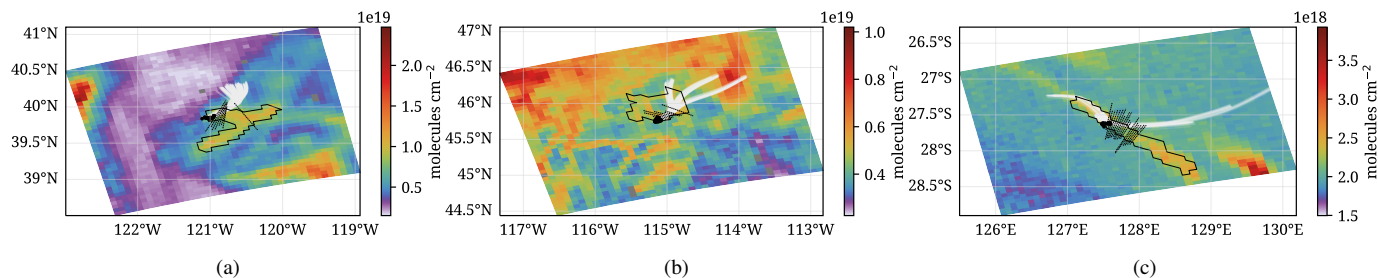
Figure 8. Removal by visual inspection. Black dots at the center of each figure, white bands and black polygon represent fire counts, tracer particles and detected plume, respectively. Black dashed lines are transaction lines. (a, b) Bad plume detection and doesn't get filtered by any of the above mentioned filters. (c) The plume and particles are oriented north-west whereas the transaction lines are drawn towards south-east which due to bad plume detection.

filter described in Section 2.3.4 removed 20 cases (11 US and 9 AU). And finally four plumes (3 US and 1 AU) were rejected by the velocity filter discussed in Sec. 2.3.4 due to velocities being lower than 2 ms^{-1}. Plumes were also visually inspected to check the quality of algorithm. A total of 3 plumes were falsely identified as shown in Fig. 8. To conclude, presented automated algorithm can successfully detect plumes and compute emissions for $\approx 97.9\%$ of the cases.

3.1 Cross-Sectional Massflux method (CFM)

3.1.1 Constant and Lagrangian plume height

The CFM was used to compute emissions for the selected 141 cases. To compare the effect of plume heights, two variables are defined, namely, mean plume height $\overline{z}_{\text{lag}}$, which is mean of z_{lag} of all transects along the downwind direction of the plume and the maximum rise in plume height (δz) w.r.t z_c. They are given as

$$\overline{z}_{\text{lag}} = \frac{1}{m} \sum_{i=0}^{m} z_{\text{lag},i} \tag{9}$$

$$\delta z = \max\{z_{\text{lag}}\} - z_c \tag{10}$$

The mean plume height $\overline{z}_{\text{lag}}$ is plotted against the constant plume height (z_c) in Figure 9(a). The δz decreased and increased in downwind direction for about 21 and 120 fires, respectively. Additionally, the plume height in the downwind direction is found to vary significantly and is highlighted by error bars in Figure 9(a). The δz was > 500 m for a total of 22 fires and are highlighted by red color points in Fig. 9(a). Among these 22 fires, about 10 fires had $\delta z > 1000$ m. As the total fire radiative power (FRP) and fire counts represent the heat generated and the area burnt, a relation between plume height rise and these two variables can be expected as higher FRP means higher temperature which heats up the air, leading rise of the warm air. However, no such relation was observed and there were cases with low FRP or low fire counts where the $\delta z > 1000$ m. However, it was difficult to find an appropriate reason for large rise in plume height in downwind direction. Obviously, this plume height variation can influence the emissions due to the change in the velocity with height.
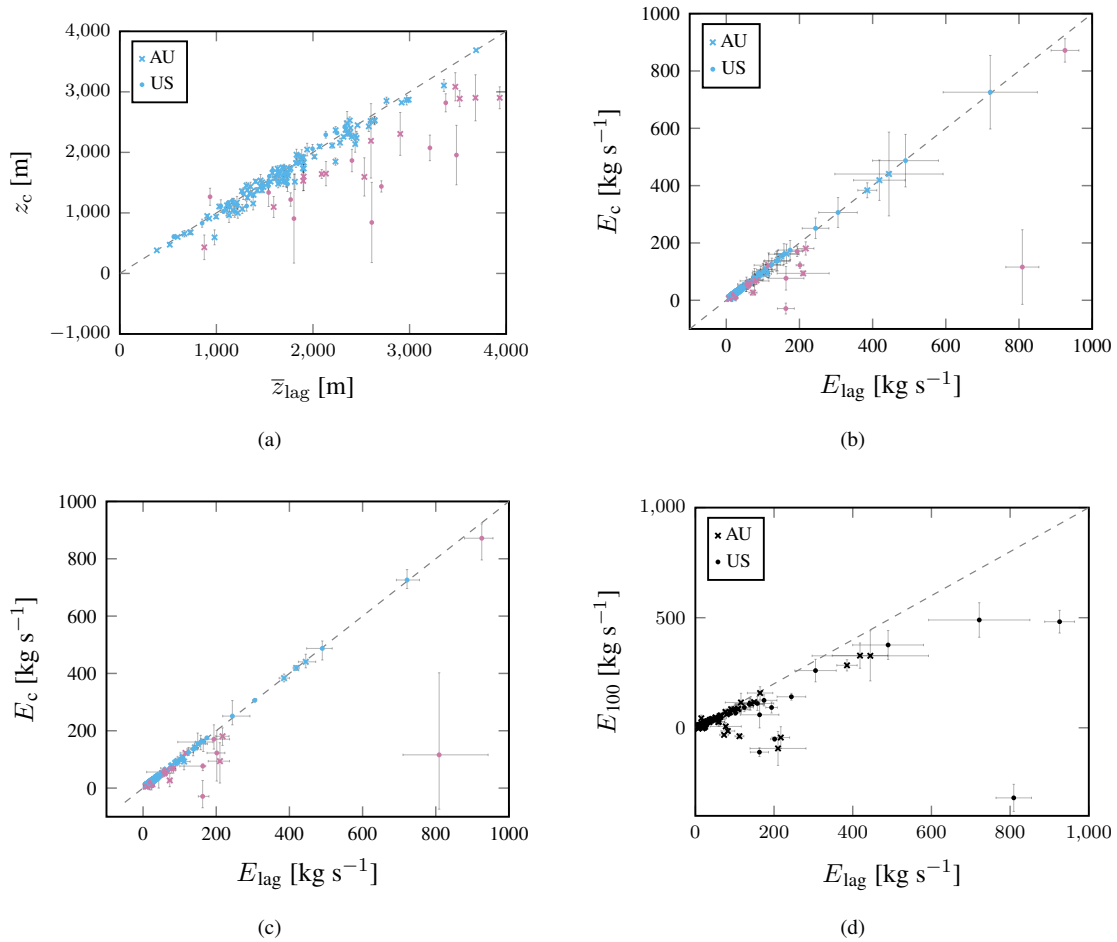
Figure 9. Plume height variation and emissions for US and Australia. (a) The mean plume height (see Eq. (9)) versus the constant plume height for each fire. The error bars indicate the standard deviation of z_{lag} in downwind direction. Reddish-purple markers indicate $\delta z \geq 500$ (see Eq. (10)) and blue indicates $\delta z < 500$. (b) Comparison between the emissions computed at plume height z_{lag} vs z_{c}. The error bars in respective direction indicate standard error E_{se} defined in Eq. (5). Colors indicate the plume height deviation (δz) shown in (a). (c) Same as Fig. (b) except the error bars show the uncertainty in emissions due to variation in plume height (z_{lag}^{p} and z_{lag}^{m}) and constant plume height (z_{c}^{p} and z_{c}^{m}). Explained in text in Section 3.2. (d) Comparison between the emissions computed at plume height z_{lag} vs the emissions at 100 m plume height, z_{100}.

A US fire (red color) on the bottom right of Figure 9(b) was found to have high $E_{\mathrm{lag}} = 809$ kgs^{-1} and low $E_{\mathrm{c}} = 115$ kgs^{-1}. The total fire radiative power (FRP) for this case was found to be the highest among all the detected plumes and the burnt area (number of fire counts in VIIRS data) was third highest among all the detected cases. Additionally, the CO enhancement was large, thus, a high emission estimate is expected. Furthermore, the high FRP is correlated with higher temperatures, so an increase in the plume height in downwind direction is normal. This is observed in the Lagrangian simulations as the z_{lag}

increases by 1350 m compared to constant plume height in the downwind direction at 32.5 km from the fire source. From this, one can conclude that the E_{lag} is more appropriate than E_{c}. A similar reasoning can be used to explain why the E_{lag} was higher by $> 30\%$ compared to E_{c} for 9 out of 22 fires where the FRP on average was higher and the δz was > 500 m. Additionally,

285 for one US fire among these 9 fires, we observe a negative E_{c} (see Figure 9(b)) due to velocities being negative at z_{c} along the plume, however the E_{lag} was found to be positive. It should also be noted that the emissions from constant plume height varied less than 10% from the Lagrangian estimate for a total of 124 cases. Thus, although the overall effect of the Lagrangian estimate of the plume height on the emission estimate is minor, we could identify several cases where the emissions estimate become more reliable.

290 ### 3.1.2 100 m plume height

Three-dimensional velocity fields are required to compute the CO emissions based on the plume heights z_{c} and z_{lag} which amounts to a large quantity of data. The approach would be much simplified when the three-dimensional velocity data could be reduced to a two-dimensional velocity field at 100 m close to the surface (Hersbach et al., 2018a). Therefore, we computed the emission also for a 100 m plume height. Figure 9(d) shows a comparison of the emissions E_{lag} computed from versus

295 a corresponding simulations $E_{100\text{m}}$ for constant plume height of 100 m. Emissions varied more than 10% with respect to Lagrangian emissions for a total of 105 cases out of 141 cases. The figure depicts large deviations between emissions and the differences increase with increasing emission. Overall $E_{100\text{m}}$ is mostly under-predicted. Additionally, $E_{100\text{m}}$ is negative for 11 fires due to a negative velocity at 100 m. Furthermore, we could not find a correlation between the difference in the emissions and the variation in plume heights. This makes it difficult to find an appropriate scaling to obtain emissions at z_{lag} from the

300 velocities at 100 m. This highlights the importance of using three-dimensional velocity fields rather than surface near wind fields at a fixed altitude.

From all these observations, we conclude that the varying plume height is more reliable to compute emissions by an automated algorithm.

3.2 Emission uncertainty

305 The error bars in figure 9(b) represent the standard error $\pm E_{\text{se}}$ defined in Equation (5). They indicate uncertainties in respective direction and encompass various uncertainty sources such as the interpolation error due to sampling (large grid sizes) in both the ERA5 velocity fields and the TROPOMI observations (shown in Fig. 5(b)), the systematic bias and precision errors in TROPOMI CO, uncertainties in defining the atmospheric CO background, the local variation in velocity fields and the assumption of a constant CO fire emission in time. These uncertainties are difficult to quantify individually as the true value is

310 unknown and the uncertainties can be different for different fires.

Figure 9(c) is the same as 9(b) except that the error bars indicate the uncertainties in emissions due to the uncertainty in plume height, which is further related to uncertainty in the injection height in GFAS database. The injection height is assumed to have an uncertainty of ± 500 m. The positive and negative error bar in x-axis correspond to two uncertainties namely, $E_{\text{lag}}^{p} - E_{\text{lag}}$ and $E_{\text{lag}} - E_{\text{lag}}^{m}$, respectively, where emissions E_{lag}^{p} and E_{lag}^{m} are computed using plume heights z_{lag}^{p} and z_{lag}^{m}, respectively

Table 2. Comparison of actual emissions to the emissions computed at plume height z_{lag} for the three selected plumes shown in Fig. 10

Time in UTC (H:M)	Actual (kgs^{-1})	1 km grid (kgs^{-1})	Tropomi grid (kgs^{-1})
17:00	28.45	20.26	20.67
18:00	56.84	34.92	34.52
19:00	97.86	99.15	99.36

315   (see Fig 7b). Similarly the uncertainties for E_c are computed. The size of the error bars highlights the variation in the velocity at different plume heights. For small error bars, this can either mean that plume height doesn't vary i.e., z^p_{lag} and z^m_{lag} converge to z_{lag}) thus low variation in velocity or plume height varies a lot but the velocity variation is low. In our case, smaller error bars were mainly observed when the velocity didn't vary much with the plume height.

An overall systematic bias in the velocity field is not computed in the presented work as it is unknown and either hard to
320   estimate or may vary for each fire. However, it should be noted that 1% systematic bias in velocity leads to a 1% error in the emission estimate due to the linearity in Eq. (4). We can assume that the localized uncertainties in velocity are covered by the standard error, E_{se}. This uncertainty quantification is also applicable to systematic biases on the whole TROPOMI CO data. The TROPOMI CO data has a positive bias of 6.5% on average compared to NDACC, TCCON, and COCCON monitoring networks (Sha et al., 2021; Lambert et al., 2022; Borsdorff et al., 2019b). It should be noted that this uncertainty has been
325   reduced to 3.4ppb in the newer versions of L2 product (Borsdorff et al., 2019b).

The CFM estimated emissions are same as actual if the emissions and velocities are constant in time. However this assumption does not hold for the fires, thus an uncertainty due to these assumptions is quantified. Additionally, as the pixel size of TROPOMI is high, the uncertainty due to low and high spatial resolutions is studied using three model cases. The Weather Research and Forecasting (WRF) simulation was performed using real atmospheric forcing at 1 km resolution for a fire with
330   the highest FRP (USA, September 12, 2020, see Sec. 3.1). The details on the WRF simulation can be found in the Appendix A. Three plumes at three different UTC times shown in Figure 10a-c were selected and emissions were estimated by our algorithm. Additionally, the simulation grid was degraded to the Tropomi grid and can be observed in Figs. 10e-g. It should be noted that the averaging kernels were not used to degrade to TROPOMI grids and only the enhancements were simulated in the model, thus the background is set to zero. The plume height (z_{lag}) was computed as the maximum height where the
335   concentration became zero and fire sources were same as the sources used in WRF simulation. The velocity used in both Lagrangian simulations and emission estimations was WRF velocity data. The emissions for these plumes were estimated by our automated plume detection and emission estimation algorithm and are presented in Table 2. The actual emission is the mean of the known total CO emission from all fire sources with time. This considered time is based on the release time of the particles around the final transect used to compute emission.

340   The highest uncertainty in cross-sectional flux method compared to actual emissions was 38.5% at UTC time 18:00 (Table 2). In all three plumes, the velocity and plume height are appropriate, however the emissions computed by our algorithm differed from the actual emissions. This is attributed to the error in the cross-sectional flux method due to the assumption of
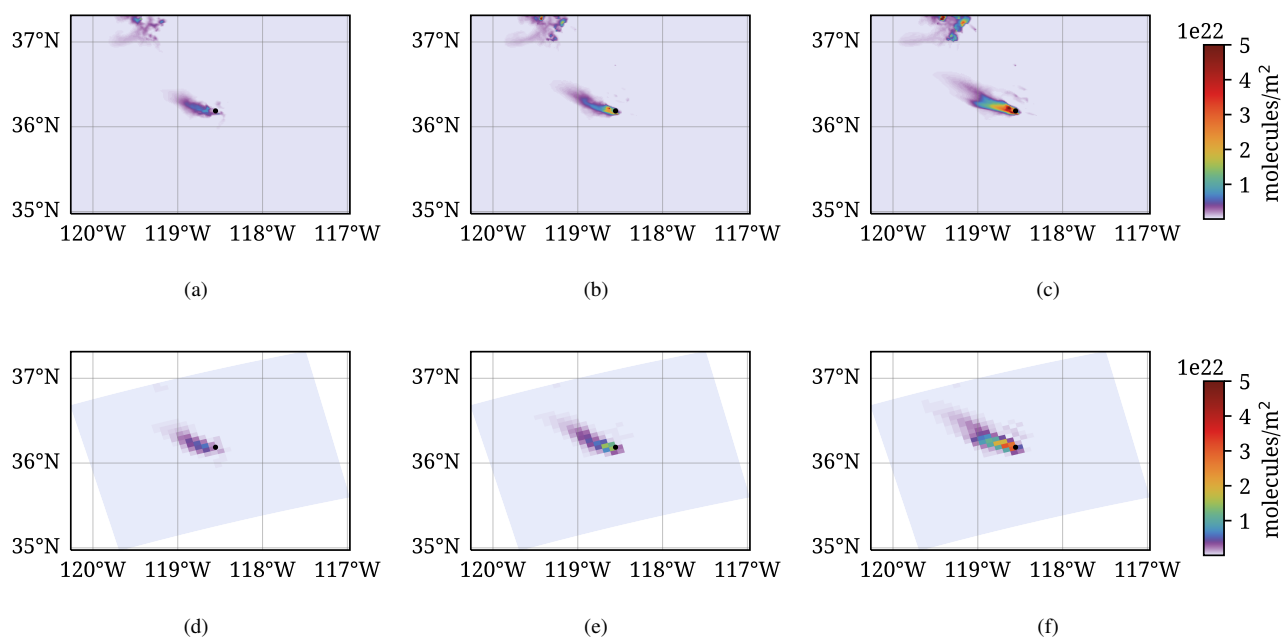
Figure 10. Three selected plumes at three different UTC times (a, d) at 17:00, (b, e) at 18:00 and (c, f) at 19:00. Top (a-c) represent plumes at 1 km grid resolution and bottom (d-f) represent TROPOMI grid resolution.

constant wind and emissions which might not be the case for a fire. It should be noted that this uncertainty is for one particular case and it can vary depending upon the case. For the three selected cases, the CFM method leads to an error of 28.8, 38.5 and

345   1.5% which highlights that even with accurate wind fields, there can be large errors depending upon the fire.

The difference in emissions between high resolution (1 km grid) and low resolution (TROPOMI grid) was found to be less than 2%. The integrated CO with distance from source as shown in 5(c) was found to be same for all three plumes for both high (1 km) and low (TROPOMI) resolution grids. If the velocity is accurate, then it can be concluded that having higher resolution data doesn't have much effect on the cross-sectional flux method.

350   **4   Conclusions and recommendations**

An automated plume detection and emission estimation scheme for CO flux inversion for fires was developed by integrating four freely available data sources, such as, VIIRS active fire dataset, TROPOMI CO dataset, injection height from GFAS and ERA5 meteorological data. The automated plume detection and emission estimation algorithm (APE v1.0) was tested for two months for US and Australia and it was shown that the fire plumes can be detected and their emissions can be estimated

355   automatically for about 97.9% of the cases.

The key to automatically detect fire plumes in TROPOMI CO dataset and estimate emissions was knowing the fire source a priori. If a fire source is not known then it is a complex problem as the CO plume in TROPOMI data needs to be identified first

and then the fire source need to computed from the identified plume. However in present study, VIIRS active fire data product from Suomi NPP helped in identifying fire source which was used to detect plumes in TROPOMI CO data. This highlights

360 the potential for flying the satellites Suomi NPP and SP5 in the same orbit and in formation with a temporal separation of 3.5 minutes to identify fires.

The emission estimation using constant plume height may not be appropriate as it doesn't include the effect of plume height variation in downwind direction. Plume height in downwind direction varied by more than 500 m for a total of 22 cases. This plume height variation could be due to variation in air temperatures caused by the fire. If the fire is at its peak then the air

365 around is heated and rises in the atmosphere and at the same time, it will be transported away from the fire source. Thus, one can observe the CO rise with distance from the source. We observed this trend in few cases where the varying plume height could give a better and reliable emission predictions compared to constant plume height. Additionally, emissions from constant plume height varied by less than 10% for 124 cases compared to Lagrangian plume height. Therefore, the overall effect of the changing plume height in downwind direction on the emission estimate was minor. However, we were able to identify several

370 cases where the flux estimates become more reliable.

The emission computed based on 100 m winds (considered plume height) were severely under-predicted due to low to negative velocities. A total of 105 cases had more than 10% variation between the emissions from 100 m plume height and the Lagrangian plume height. It was difficult to find an appropriate scaling of velocity at 100 m to the velocity at plume height z_{lag} as the negative velocities cannot be scaled to positive velocity. Additionally, in many cases the velocity was found to be

375 constant with height thus using a general scaling factor to scale velocity with height might result in unrealistic emissions.

The combined effect of uncertainties due to different parameters is difficult to quantify for fires due to the missing ground truth. The CFM was found to have significant uncertainties compared to actual emissions for fires even though the atmospheric transport and plume height considered were accurate. This stems from the CFM assumptions of constant emissions and velocity in time which is not the case for fires. Additionally, as the uncertainty can vary from a fire to another, it is difficult to quantify

380 it in an automated way.

Finally, for the first time the presented algorithm is appropriate to estimate CO emissions from fires from TROPOMI/VIIRS data by a fully automated algorithm. We identified the assumption of constant wind and emissions in time for the CFM as one of the significant contributor to the uncertainty in our data product.

As a next step, (1) the entire CO TROPOMI data set will be processed and (2) develop an improved inversion scheme. This

385 can done by developing algorithms that maps the simulated tracer particles from Lagrangian simulations to the TROPOMI CO concentrations to compute emissions. Thus, including the history of the emissions to a certain extent. (3) A database of the fires with single sources will be created and further studied to understand the effect of vegetation and topography.

Appendix A: The Weather Research and Forecasting (WRF) Model description

The WRF model configured in a two-domain configuration is applied in the tracer mode to simulate the transport and dispersion

390 of CO emitted by a wildfire in the US. The outer and inner domains are run at a horizontal grid spacing of 5×5 km^2 and 1×1

km^2, respectively. The model domains are centered at 36.16225^0N, 119.1528^0E and have 43 vertical levels stretching from the surface to a model top of 50 hPa. The outer domain has 200×200 grid points while the inner domain has 400×350 grid points in the west-east and north-south directions. The meteorological initial and boundary conditions for the outer domain are based on the Global Forecast System (GFS) forecasts available every 3 hours at a horizontal grid spacing of $0.25^0 \times 0.25^0$.

395   The static geographical fields and the GFS output are mapped onto the WRF domains using the WRF pre-processing system (WPS). The physical parameterizations follow Kumar et al. (2021) except the cumulus parameterization that is turned off in the inner domain.

Biomass burning emissions are obtained from the Fire Inventory from NCAR (FINN; Wiedinmyer et al., 2011) version 2.5 and are distributed vertically online using a plume rise parameterization developed by Freitas et al. (2007). This parameteri-

400   zation selects fire properties appropriate for the land use in every grid box containing fire emissions and simulates the plume rise explicitly using the environmental conditions simulated by WRF. Since we are using the model in the tracer mode, the chemical evolution of the plume is not simulated. To describe the loss of CO in the model, we allow the CO fire emissions to decay with an e-folding lifetime of 30 days. No other source (anthropogenic emissions, biogenic emissions or photochemical production from hydrocarbons) is included in the simulation. The model run started on 12 Sep 2020 at 12 UTC and stopped

405   at 13 Sep 00 UTC. We used a time step of 20 s for the outer domain and 4 s for the inner domain. The model output is saved every min and used for further analysis.

Code availability. APE v1.0 code is archived on Zenodo (https://doi.org/10.5281/zenodo.7374361).

Data availability. The TROPOMI CO dataset of this study is available for download at ftp://ftp.sron.nl/open-access-data-2/TROPOMI/tropomi/co/ (last access: 10 October 2020). The IS4FIRES injection height and the 3-d velocities at 127 model levels were obtained from the Global Fire

410   Assimilation System (GFAS) database and the European Center for Medium range Weather Forecasts (ECMWF) Reanalysis v5 (ERA5), respectively on 10 October 2020. The Visible Infrared Imaging Radiometer Suite 375m thermal anomalies/active fire product was also accessed on October 2020 (https://firms.modaps.eosdis.nasa.gov/active_fire/). The processed data will also be made available on the request of the editor.

Author contributions. MG developed the code and performed analysis with the inputs from TB and JL. JA master thesis served as feasibility

415   study for this work. RK performed WRF simulations and gave inputs on its data analysis. All co-authors commented and improved the paper with a special mention to JL and TB.

Competing interests. The authors declare that they have no conflict of interest.

Acknowledgements. The National Center for Atmospheric Research is sponsored by the National Science Foundation.

References

420 Andreae, M. O., Browell, E. V., Garstang, M., Gregory, G. L., Harriss, R. C., Hill, G. F., Jacob, D. J., Pereira, M. C., Sachse, G. W., Setzer, A. W., Dias, P. L. S., Talbot, R. W., Torres, A. L., and Wofsy, S. C.: Biomass-burning emissions and associated haze layers over Amazonia, Journal of Geophysical Research, 93, 1509, https://doi.org/10.1029/jd093id02p01509, 1988.

Apituley, A., Pedergnana, M., Sneep, M., Veefkind, J. P., Loyola, D., Landgraf, J., and Borsdorff, T.: Sentinel-5 precursor/TROPOMI Level 2 Product User Manual Carbon Monoxide, User Manual SRON-S5P-LEV2-MA-002, 1.0.0, SRON Netherlands Institute for Space Research,
425 Leiden, The Netherlands, 2018.

Beare, R.: A locally constrained watershed transform, IEEE Transactions on Pattern Analysis and Machine Intelligence, 28, 1063–1074, https://doi.org/10.1109/tpami.2006.132, 2006.

Beirle, S., Boersma, K. F., Platt, U., Lawrence, M. G., and Wagner, T.: Megacity Emissions and Lifetimes of Nitrogen Oxides Probed from Space, Science, 333, 1737–1739, https://doi.org/10.1126/science.1207824, 2011.

430 Bey, I., Jacob, D. J., Yantosca, R. M., Logan, J. A., Field, B. D., Fiore, A. M., Li, Q., Liu, H. Y., Mickley, L. J., and Schultz, M. G.: Global modeling of tropospheric chemistry with assimilated meteorology: Model description and evaluation, Journal of Geophysical Research: Atmospheres, 106, 23 073–23 095, https://doi.org/10.1029/2001jd000807, 2001.

Borsdorff, T., de Brugh, J. A., Hu, H., Aben, I., Hasekamp, O., and Landgraf, J.: Measuring Carbon Monoxide With TROPOMI: First Results and a Comparison With ECMWF-IFS Analysis Data, Geophysical Research Letters, 45, 2826–2832,
435 https://doi.org/10.1002/2018gl077045, 2018.

Borsdorff, T., aan de Brugh, J., Pandey, S., Hasekamp, O., Aben, I., Houweling, S., and Landgraf, J.: Carbon monoxide air pollution on sub-city scales and along arterial roads detected by the Tropospheric Monitoring Instrument, Atmospheric Chemistry and Physics, 19, 3579–3588, https://doi.org/10.5194/acp-19-3579-2019, 2019a.

Borsdorff, T., aan de Brugh, J., Schneider, A., Lorente, A., Birk, M., Wagner, G., Kivi, R., Hase, F., Feist, D. G., Sussmann, R., Rettinger, M.,
440 Wunch, D., Warneke, T., and Landgraf, J.: Improving the TROPOMI CO data product: update of the spectroscopic database and destriping of single orbits, Atmospheric Measurement Techniques, 12, 5443–5455, https://doi.org/10.5194/amt-12-5443-2019, 2019b.

Borsdorff, T., García Reynoso, A., Maldonado, G., Mar-Morales, B., Stremme, W., Grutter, M., and Landgraf, J.: Monitoring CO emissions of the metropolis Mexico City using TROPOMI CO observations, Atmospheric Chemistry and Physics Discussions, pp. 1–21, https://doi.org/10.5194/acp-2020-238, 2020.

445 Brasseur, G. P. and Jacob, D. J.: Modeling of Atmospheric Chemistry, Cambridge University Press, https://doi.org/10.1017/9781316544754, 2017.

Brunner, D., Kuhlmann, G., Marshall, J., Clément, V., Fuhrer, O., Broquet, G., Löscher, A., and Meijer, Y.: Accounting for the vertical distribution of emissions in atmospheric CO_2 simulations, Atmospheric Chemistry and Physics, 19, 4541–4559, https://doi.org/10.5194/acp-19-4541-2019, 2019.

450 Cambaliza, M. O. L., Shepson, P. B., Caulton, D. R., Stirm, B., Samarov, D., Gurney, K. R., Turnbull, J., Davis, K. J., Possolo, A., Karion, A., Sweeney, C., Moser, B., Hendricks, A., Lauvaux, T., Mays, K., Whetstone, J., Huang, J., Razlivanov, I., Miles, N. L., and Richardson, S. J.: Assessment of uncertainties of an aircraft-based mass balance approach for quantifying urban greenhouse gas emissions, Atmospheric Chemistry and Physics, 14, 9029–9050, https://doi.org/10.5194/acp-14-9029-2014, 2014.

Cambaliza, M. O. L., Shepson, P. B., Bogner, J., Caulton, D. R., Stirm, B., Sweeney, C., Montzka, S. A., Gurney, K. R., Spokas, K.,
455 Salmon, O. E., Lavoie, T. N., Hendricks, A., Mays, K., Turnbull, J., Miller, B. R., Lauvaux, T., Davis, K., Karion, A., Moser, B., Miller,

C., Obermeyer, C., Whetstone, J., Prasad, K., Miles, N., and Richardson, S.: Quantification and source apportionment of the methane emission flux from the city of Indianapolis, Elementa: Science of the Anthropocene, 3, https://doi.org/10.12952/journal.elementa.000037, 2015.

Crippa, M., Guizzardi, D., Muntean, M., Schaaf, E., Dentener, F., van Aardenne, J. A., Monni, S., Doering, U., Olivier, J. G. J., Pagliari, V.,
460   and Janssens-Maenhout, G.: Gridded emissions of air pollutants for the period 1970–2012 within EDGAR v4.3.2, Earth System Science Data, 10, 1987–2013, https://doi.org/10.5194/essd-10-1987-2018, 2018.

Ester, M., Kriegel, H.-P., Sander, J., and Xu, X.: A Density-Based Algorithm for Discovering Clusters in Large Spatial Databases with Noise, pp. 226–231, From: KDD-96 Proceedings. Copyright © 1996, AAAI (www.aaai.org). All rights reserved., 1996.

Finch, D., Palmer, P., and Zhang, T.: Automated detection of atmospheric NO_2 plumes from satellite data: a tool to help infer anthropogenic
465   combustion emissions, Atmospheric Measurement Techniques Discussions, 2021, 1–21, https://doi.org/10.5194/amt-2021-177, 2021.

Fiorio, C. and Gustedt, J.: Two linear time Union-Find strategies for image processing, Theoretical Computer Science, 154, 165–181, https://doi.org/10.1016/0304-3975(94)00262-2, 1996.

Frankenberg, C., Thorpe, A. K., Thompson, D. R., Hulley, G., Kort, E. A., Vance, N., Borchardt, J., Krings, T., Gerilowski, K., Sweeney, C., Conley, S., Bue, B. D., Aubrey, A. D., Hook, S., and Green, R. O.: Airborne methane remote measurements re-
470   veal heavy-tail flux distribution in Four Corners region, Proceedings of the National Academy of Sciences, 113, 9734–9739, https://doi.org/10.1073/pnas.1605617113, 2016.

Freitas, S. R., Longo, K. M., Chatfield, R., Latham, D., Dias, M. A. F. S., Andreae, M. O., Prins, E., Santos, J. C., Gielow, R., and Carvalho, J. A.: Including the sub-grid scale plume rise of vegetation fires in low resolution atmospheric transport models, Atmospheric Chemistry and Physics, 7, 3385–3398, https://doi.org/10.5194/acp-7-3385-2007, 2007.

475   Gao, H., Xue, P., and Lin, W.: A new marker-based watershed algorithm, in: 2004 IEEE International Symposium on Circuits and Systems (IEEE Cat. No.04CH37512), vol. 2, IEEE, IEEE, https://doi.org/10.1109/iscas.2004.1329213, 2004.

Granier, C., Bessagnet, B., Bond, T., D'Angiola, A., van der Gon, H. D., Frost, G. J., Heil, A., Kaiser, J. W., Kinne, S., Klimont, Z., Kloster, S., Lamarque, J.-F., Liousse, C., Masui, T., Meleux, F., Mieville, A., Ohara, T., Raut, J.-C., Riahi, K., Schultz, M. G., Smith, S. J., Thompson, A., van Aardenne, J., van der Werf, G. R., and van Vuuren, D. P.: Evolution of anthropogenic and biomass burning emissions of air
480   pollutants at global and regional scales during the 1980–2010 period, Climatic Change, 109, 163–190, https://doi.org/10.1007/s10584-011-0154-1, 2011.

Grell, G. A., Peckham, S. E., Schmitz, R., McKeen, S. A., Frost, G., Skamarock, W. C., and Eder, B.: Fully coupled "online" chemistry within the WRF model, Atmospheric Environment, 39, 6957–6975, https://doi.org/10.1016/j.atmosenv.2005.04.027, 2005.

Hersbach, H., Bell, B., Berrisford, P., Biavati, G., Horányi, A., Muñoz Sabater, J., Nicolas, J., Peubey, C., Radu, R., Rozum, I., Schepers, D.,
485   Simmons, A., Soci, C., Dee, D., and Thépaut, J.-N.: ERA5 hourly data on single levels from 1979 to present., Copernicus Climate Change Service (C3S) Climate Data Store (CDS), https://doi.org/10.24381/cds.adbb2d47, accessed on 10-10-2020, 2018a.

Hersbach, H., Bell, B., Berrisford, P., Biavati, G., Horányi, A., Muñoz Sabater, J., Nicolas, J., Peubey, C., Radu, R., Rozum, I., Schepers, D., Simmons, A., Soci, C., Dee, D., and Thépaut, J.-N.: ERA5 model level parameters: instantaneous., Copernicus Climate Change Service (C3S) Climate Data Store (CDS), accessed on 10-10-2020, 2018b.

490   Hoesly, R. M., Smith, S. J., Feng, L., Klimont, Z., Janssens-Maenhout, G., Pitkanen, T., Seibert, J. J., Vu, L., Andres, R. J., Bolt, R. M., Bond, T. C., Dawidowski, L., Kholod, N., ichi Kurokawa, J., Li, M., Liu, L., Lu, Z., Moura, M. C. P., O'Rourke, P. R., and Zhang, Q.: Historical (1750–2014) anthropogenic emissions of reactive gases and aerosols from the Community Emissions Data System (CEDS), Geoscientific Model Development, 11, 369–408, https://doi.org/https://doi.org/10.5194/gmd-11-369-2018, 2018.

Holloway, T., Levy, H., and Kasibhatla, P.: Global distribution of carbon monoxide, Journal of Geophysical Research: Atmospheres, 105, 12 123–12 147, https://doi.org/10.1029/1999jd901173, 2000.

Krings, T., Gerilowski, K., Buchwitz, M., Reuter, M., Tretner, A., Erzinger, J., Heinze, D., Pflüger, U., Burrows, J. P., and Bovensmann, H.: MAMAP – a new spectrometer system for column-averaged methane and carbon dioxide observations from aircraft: retrieval algorithm and first inversions for point source emission rates, Atmospheric Measurement Techniques, 4, 1735–1758, https://doi.org/https://doi.org/10.5194/amt-4-1735-2011, 2011.

Kuhlmann, G., Broquet, G., Marshall, J., Clément, V., Löscher, A., Meijer, Y., and Brunner, D.: Detectability of CO_2 emission plumes of cities and power plants with the Copernicus Anthropogenic CO_2 Monitoring (CO2M) mission, Atmospheric Measurement Techniques, 12, 6695–6719, https://doi.org/https://doi.org/10.5194/amt-12-6695-2019, 2019.

Kuhlmann, G., Brunner, D., Broquet, G., and Meijer, Y.: Quantifying CO_2 Monitoring satellite mission emissions of a city with the Copernicus Anthropogenic CO_2 Monitoring satellite mission, Atmospheric Measurement Techniques, 13, 6733–6754, https://doi.org/10.5194/amt-13-6733-2020, 2020.

Kumar, R., Bhardwaj, P., Pfister, G., Drews, C., Honomichl, S., and D'Attilo, G.: Description and Evaluation of the Fine Particulate Matter Forecasts in the NCAR Regional Air Quality Forecasting System, Atmosphere, 12, 302, https://doi.org/10.3390/atmos12030302, 2021.

Lama, S., Houweling, S., Boersma, K. F., Eskes, H., Aben, I., Denier van der Gon, H. A. C., Krol, M. C., Dolman, H., Borsdorff, T., and Lorente, A.: Quantifying burning efficiency in megacities using the NO_2/CO ratio from the Tropospheric Monitoring Instrument (TROPOMI), Atmospheric Chemistry and Physics, 20, 10 295–10 310, https://doi.org/10.5194/acp-20-10295-2020, 2020.

Lambert, J.-C., Keppens, A., Compernolle, S., Eichmann, K.-U., de Graaf, M., Hubert, D., Langerock, B., Ludewig, A., Sha, M. K., Verhoelst, T., Wagner, T., Ahn, C., Argyrouli, A., Balis, D., Chan, K. L., Smedt, I. D., Eskes, H., Fjæraa, A. M., Garane, K., Gleason, J. F., Goutail, F., Granville, J., Hedelt, P., Heue, K.-P., Jaross, G., Kleipool, Q., Koukouli, M. L., Lorente, A., Lutz, R., Nanda, S., S.Niemeijer, Pazmiño, A., Pinardi, G., Pommereau, J.-P., Richter, A., Rozemeijer, N., Sneep, M., Zweers, D. S., Theys, N., Tilstra, G., Torres, O., Valks, P., vanGeffen, J., Vigouroux, C., Wang, P., and Weber, M.: Quarterly validation report of the copernicus sentinel-5 precursor operational data products #14: april 2018 – march 2022, S5P MPC Routine Operations Consolidated Validation Report (ROCVR) 14.01.01, https://mpc-vdaf.tropomi.eu/, 2022.

Lee, B., Cho, S., Lee, S.-K., Woo, C., and Park, J.: Development of a Smoke Dispersion Forecast System for Korean Forest Fires, Forests, 10, 219, https://doi.org/10.3390/f10030219, 2019.

Li, F., Zhang, X., Kondragunta, S., and Lu, X.: An evaluation of advanced baseline imager fire radiative power based wildfire emissions using carbon monoxide observed by the Tropospheric Monitoring Instrument across the conterminous United States, Environmental Research Letters, 15, 094 049, https://doi.org/10.1088/1748-9326/ab9d3a, 2020.

Lorente, A., Borsdorff, T., Butz, A., Hasekamp, O., aan de Brugh, J., Schneider, A., Wu, L., Hase, F., Kivi, R., Wunch, D., Pollard, D. F., Shiomi, K., Deutscher, N. M., Velazco, V. A., Roehl, C. M., Wennberg, P. O., Warneke, T., and Landgraf, J.: Methane retrieved from TROPOMI: improvement of the data product and validation of the first 2 years of measurements, Atmospheric Measurement Techniques, 14, 665–684, https://doi.org/10.5194/amt-14-665-2021, 2021.

Magro, C., Nunes, L., Gonçalves, O., Neng, N., Nogueira, J., Rego, F., and Vieira, P.: Atmospheric Trends of CO and CH4 from Extreme Wildfires in Portugal Using Sentinel-5P TROPOMI Level-2 Data, Fire, 4, 25, https://doi.org/10.3390/fire4020025, 2021.

Nassar, R., Hill, T. G., McLinden, C. A., Wunch, D., Jones, D. B. A., and Crisp, D.: Quantifying CO_2 Emissions From Individual Power Plants From Space, Geophysical Research Letters, 44, https://doi.org/10.1002/2017gl074702, 2017.

Pedregosa, F., Varoquaux, G., Gramfort, A., Michel, V., Thirion, B., Grisel, O., Blondel, M., Prettenhofer, P., Weiss, R., Dubourg, V., Vanderplas, J., Passos, A., Cournapeau, D., Brucher, M., Perrot, M., and Duchesnay, E.: Scikit-learn: Machine Learning in Python, Journal of Machine Learning Research, 12, 2825–2830, 2011.

535 Rémy, S., Veira, A., Paugam, R., Sofiev, M., Kaiser, J. W., Marenco, F., Burton, S. P., Benedetti, A., Engelen, R. J., Ferrare, R., and Hair, J. W.: Two global data sets of daily fire emission injection heights since 2003, Atmospheric Chemistry and Physics, 17, 2921–2942, https://doi.org/10.5194/acp-17-2921-2017, 2017.

Rowe, J. P., Zarzana, K. J., Kille, N., Borsdorff, T., Goudar, M., Lee, C. F., Koenig, T. K., Romero-Alvarez, J., Campos, T., Knote, C., Theys, N., Landgraf, J., and Volkamer, R.: Carbon Monoxide in Optically Thick Wildfire Smoke: Evaluating TROPOMI Using CU Airborne SOF Column Observations, ACS Earth and Space Chemistry, 6, 1799–1812, https://doi.org/10.1021/acsearthspacechem.2c00048, 2022.

540 Schneising, O., Buchwitz, M., Reuter, M., Bovensmann, H., and Burrows, J. P.: Severe Californian wildfires in November 2018 observed from space: the carbon monoxide perspective, Atmospheric Chemistry and Physics, 20, 3317–3332, https://doi.org/10.5194/acp-20-3317-2020, 2020.

Schroeder, W., Oliva, P., Giglio, L., and Csiszar, I. A.: The New VIIRS 375 m active fire detection data product: Algorithm description and initial assessment, Remote Sensing of Environment, 143, 85–96, https://doi.org/10.1016/j.rse.2013.12.008, 2014.

545 Schubert, E., Sander, J., Ester, M., Kriegel, H. P., and Xu, X.: DBSCAN Revisited, Revisited, ACM Transactions on Database Systems, 42, 1–21, https://doi.org/10.1145/3068335, 2017.

Sha, M. K., Langerock, B., Blavier, J.-F. L., Blumenstock, T., Borsdorff, T., Buschmann, M., Dehn, A., Mazière, M. D., Deutscher, N. M., Feist, D. G., García, O. E., Griffith, D. W. T., Grutter, M., Hannigan, J. W., Hase, F., Heikkinen, P., Hermans, C., Iraci, L. T., Jeseck, P., Jones, N., Kivi, R., Kumps, N., Landgraf, J., Lorente, A., Mahieu, E., Makarova, M. V., Mellqvist, J., Metzger, J.-M., Morino, I., 550 Nagahama, T., Notholt, J., Ohyama, H., Ortega, I., Palm, M., Petri, C., Pollard, D. F., Rettinger, M., Robinson, J., Roche, S., Roehl, C. M., Röhling, A. N., Rousogenous, C., Schneider, M., Shiomi, K., Smale, D., Stremme, W., Strong, K., Sussmann, R., Té, Y., Uchino, O., Velazco, V. A., Vigouroux, C., Vrekoussis, M., Wang, P., Warneke, T., Wizenberg, T., Wunch, D., Yamanouchi, S., Yang, Y., and Zhou, M.: Validation of methane and carbon monoxide from Sentinel-5 Precursor using TCCON and NDACC-IRWG stations, Atmospheric Measurement Techniques, 14, 6249–6304, https://doi.org/10.5194/amt-14-6249-2021, 2021.

555 Shi, Y., Matsunaga, T., and Yamaguchi, Y.: High-Resolution Mapping of Biomass Burning Emissions in Three Tropical Regions, Environmental Science & Technology, 49, 10 806–10 814, https://doi.org/10.1021/acs.est.5b01598, 2015.

Sobel, I. and Feldman, G. M.: An Isotropic 3×3 image gradient operator, 1990.

Sofiev, M., Ermakova, T., and Vankevich, R.: Evaluation of the smoke-injection height from wild-land fires using remote-sensing data, Atmospheric Chemistry and Physics, 12, 1995–2006, https://doi.org/10.5194/acp-12-1995-2012, 2012.

560 Spivakovsky, C. M., Logan, J. A., Montzka, S. A., Balkanski, Y. J., Foreman-Fowler, M., Jones, D. B. A., Horowitz, L. W., Fusco, A. C., Brenninkmeijer, C. A. M., Prather, M. J., Wofsy, S. C., and McElroy, M. B.: Three-dimensional climatological distribution of tropospheric OH: Update and evaluation, Journal of Geophysical Research: Atmospheres, 105, 8931–8980, https://doi.org/10.1029/1999jd901006, 2000.

Tian, Y., Sun, Y., Borsdorff, T., Liu, C., Liu, T., Zhu, Y., Yin, H., and Landgraf, J.: Quantifying CO emission rates of industrial point sources 565 from TROPOMI observations, Environmental Research Letters, https://doi.org/10.1088/1748-9326/ac3b1a, 2021.

van der Velde, I. R., van der Werf, G. R., Houweling, S., Maasakkers, J. D., Borsdorff, T., Landgraf, J., Tol, P., van Kempen, T. A., van Hees, R., Hoogeveen, R., Veefkind, J. P., and Aben, I.: Vast CO2 release from Australian fires in 2019–2020 constrained by satellite, Nature, 597, 366–369, https://doi.org/10.1038/s41586-021-03712-y, 2021.

van der Walt, S., Schönberger, J. L., Nunez-Iglesias, J., Boulogne, F., Warner, J. D., Yager, N., Gouillart, E., and Yu, T.: scikit-image: Image processing in Python, PeerJ, 2, e453, https://doi.org/10.7717/peerj.453, 2014.

Varon, D. J., Jacob, D. J., McKeever, J., Jervis, D., Durak, B. O. A., Xia, Y., and Huang, Y.: Quantifying methane point sources from fine-scale satellite observations of atmospheric methane plumes, Atmospheric Measurement Techniques, 11, 5673–5686, https://doi.org/10.5194/amt-11-5673-2018, 2018.

Watson, C. E., Fishman, J., and Reichle, H. G.: The significance of biomass burning as a source of carbon monoxide and ozone in the southern hemisphere tropics: A satellite analysis, Journal of Geophysical Research, 95, 16 443, https://doi.org/https://doi.org/10.1029/JD095iD10p16443, 1990.

White, W. H., Anderson, J. A., Blumenthal, D. L., Husar, R. B., Gillani, N. V., Husar, J. D., and Wilson, W. E.: Formation and Transport of Secondary Air Pollutants: Ozone and Aerosols in the St. Louis Urban Plume, Science, 194, 187–189, https://doi.org/10.1126/science.959846, 1976.

Wiedinmyer, C., Akagi, S. K., Yokelson, R. J., Emmons, L. K., Al-Saadi, J. A., Orlando, J. J., and Soja, A. J.: The Fire INventory from NCAR (FINN): a high resolution global model to estimate the emissions from open burning, Geoscientific Model Development, 4, 625–641, https://doi.org/10.5194/gmd-4-625-2011, 2011.